Title

Effects of the distribution and evolution of the coefficient of friction along a fault on the assessment of the seismic activity associated with a hypothetical industrial-scale geologic CO2 sequestration operation

Authors

Jeanne, Pierre
Rutqvist, Jonny
Foxall, William
et al.

Publication Date

2017-11-01

DOI

10.1016/j.ijggc.2017.09.018

Peer reviewed

International Journal of Greenhouse Gas Control 66 (2017) 254–263

Contents lists available at ScienceDirect

International Journal of Greenhouse Gas Control

journal homepage: www.elsevier.com/locate/ijggc

Effects of the distribution and evolution of the coefficient of friction along a fault on the assessment of the seismic activity associated with a hypothetical industrial-scale geologic CO_2 sequestration operation

Pierre Jeanne[a,*], Jonny Rutqvist[a], William Foxall[a], Antonio Pio Rinaldi[b], Haruko M. Wainwright[a], Quanlin Zhou[a], Jens Birkholzer[a], Corinne Layland-Bachmann[a]

[a] Lawrence Berkeley National Laboratory, Energy Geoscience Division, Berkeley, CA, 94720, USA
[b] Swiss Seismological Service, Swiss Federal Institute of Technology, ETHZ, Zürich, Switzerland

ARTICLE INFO

Keywords:
CO_2 sequestration
Geomechanical simulations
Induced seismicity
Coefficient of friction

ABSTRACT

Carbon capture and storage (CCS) in geological formations is considered as a promising option that could limit CO_2 emissions from human activities into the atmosphere. However, there is a risk that pressure buildup inside the storage formation can induce slip along preexisting faults and create seismic event felt by the population. To prevent this to happen a geomechanical fault stability analysis should be performed, considering uncertainties of input parameters. In this paper, we investigate how the distribution of the coefficient of friction and the applied frictional law could influence the assessment of fault stability and the characteristics of potential injection-induced seismic events. Our modelling study is based on a hypothetical industrial-scale carbon sequestration project located in the Southern San Joaquin Basin in California, USA, where the stability on a major (25 km long) fault that bounds the sequestration site is assessed during 50 years of CO_2 injection. We conduct nine simulations in which the distributions of the coefficients of static and dynamic friction are changed to simulate a hardening and softening phase before and during rupture. Our main findings are: (i) variations in friction along the fault have an important effect on the predicted seismic activity, with maximum magnitude ranging from 1.88 to 5.88 and number of seismic events ranging from 338 to 3272; (ii) the extreme values of the coefficient of friction (lowest and highest) present along the rupture area control how much stress is accumulated before rupture; and (iii) an argillaceous caprock can prevent the development of large magnitude seismic events but favor the occurrence of a large number of smaller events.

1. Introduction

Geologic Carbon Sequestration (GCS) has been recognized as a promising option for reducing CO_2 emissions from large stationary sources (Pacala and Socolow, 2004). However, large amounts of CO_2 (several billions of tons per years over several decades) have to be stored in deep geological formations before GCS has the desired beneficial effect on climate change (Zoback and Gorelick, 2012). One main challenge is that projects involving large net volumes of fluid injection over long periods of time (such as GCS) may have the potential to induce seismic events of concern (National Research Council, 2012). The magnitudes of induced events depend on a number of parameters such as fault orientation, stress field, injection location relative to the fault, and rock and fault properties (Rutqvist et al., 2016). However, considerable uncertainties are usually associated with these parameters and could strongly influence the prediction of the overall induced seismic activity. Jeanne et al. (2016) studied the effects of in-situ stress measurement uncertainties on the assessment of the seismic activity and risk associated with a hypothetical industrial-scale geologic CO_2 sequestration operation. They suggested that the uncertainty on the stress state, as defined by the range of stresses obtained during in-situ stress measurements at that particular site, had a negligible effect on the prediction of the maximum magnitude, but an important effect the seismicity rate (number of seismic events) and the timing and location of seismic activity. This paper is a natural continuation of the study presented in Jeanne et al. (2016) using the same approach and models. Here, we investigate how the representation of the frictional strength of the fault influences the assessment of the seismic activity.

Laboratory studies show that a tangential shear stress (τ) applied parallel to a fault or fracture in a rock sample subject to a normal load (σ) must reach some critical value in order for sliding to occur (Amontons, 1699). The relation between τ and σ may be written as

* Corresponding author.
E-mail address: pjeanne@lbl.gov (P. Jeanne).

http://dx.doi.org/10.1016/j.ijggc.2017.09.018
Received 12 September 2016; Received in revised form 25 September 2017; Accepted 25 September 2017
1750-5836/ Published by Elsevier Ltd.

$\tau = c + \mu_s\sigma$ (Coulomb, 1773), with c the cohesion. Because this equation refers to the condition necessary to initiate sliding starting from a state of rest, μ_s is called the coefficient of static friction. Frictional sliding experiments show that μ_s typically ranges from 0.6 to 0.85 for a large variety of rocks (Byerlee, 1978), but μ_s decreases with increasing clay content (Lockner and Beeler, 2002; Moore and Lockner, 2007; Tembe et al., 2010) and can be as low as 0.3 in clay-bearing fault gouge (Morrow et al., 2007; Solum et al., 2006). Once sliding has been initiated the friction evolves with increasing slip and slip rate towards the coefficient of dynamic friction, μ_d. Laboratory experiments usually show that when the sliding velocity is increased μ_d increases (hardening) before decreasing (softening), potentially resulting in unstable (seismic) slip (Marone, 1998). Ideally, when assessing the seismic hazard along faults located in the vicinity of a potential geological CO_2 storage site, dynamic numerical models must consider these variations of the coefficient of friction but also:

(i) The geometrical characteristic of the reservoir and surrounding rock formations
(ii) fault zone orientation (dip and strike)
(iii) fault zone architecture (damage zone and fault core)
(iv) hydraulic and mechanical properties of the different geological layers within the host rock and the fault zone
(v) initial in situ stress regime (magnitude and orientation)
(vi) spatial distribution and evolution of the fluid pore pressure and CO_2 saturation
(vii) adequate equation(s) describing changes in permeability associated with the induced deformation

However, our ability to perform such numerical modelling is restricted by the actual limitation of the numerical tool. Indeed, the simulation of both quasi-static and dynamic phenomena using a large numerical grid with variable grid size is very time-consuming and requires significant computational power. When modeling induced seismicity, seismologists have commonly used a simple flow model and represented pre-existing faults and fractures over the modelling domain with a random distribution of their parameters (such as fracture orientation or extent, friction parameters, stress parameters, etc.) (Bachmann et al., 2012; Catalli et al., 2016; Gischig and Wiemer, 2013; Goertz-Allmann et al., 2011; Shapiro et al., 2007), but in some cases the rate-and-state friction law is used to fully describe friction evolution on discrete faults (Dieterich et al., 2015; McClure and Horne, 2011). Conversely, geomechanical studies commonly focus more on the geology, the fault zone architecture, the distribution of the hydro-mechanical properties and the multiphase fluid flow and coupled hydro-geomechanical processes. On the other hand, the coefficient of static friction is often considered as homogeneously distributed along the fault with a linear strain-softening frictional law with a residual coefficient of dynamic friction as low as 0.2 to simulate a sudden slip (Cappa and Rutqvist, 2011; Figueiredo et al., 2015; Jeanne et al., 2014; Mazzoldi et al., 2012; Rinaldi et al., 2014; Rutqvist et al., 2014).

In this paper, we linked a basin-scale coupled multiphase fluid flow simulation with a high resolution geomechanical model of a major reservoir-bounding fault. We develop different scenarios in which the fault strength is changed and analyze geomechanical fault stability response during a hypothetical carbon sequestration project initially planned at an industrial-scale in the Southern San Joaquin Basin in California, USA (Fig. 1a) (Birkholzer et al., 2011; Wainwright et al., 2013; Zhou and Birkholzer, 2011). We conduct nine simulations in which the distribution of the coefficients of static and dynamic friction are changed to simulated a hardening and softening phase before and during rupture.

2. Geological setting

The hypothetical industrial-scale carbon sequestration project is located in the center of the San Joaquin Basin. The targeted storage formation is the Vedder Sand and the overlying Freeman-Jewell Shale is the caprock (Fig. 1). Table 1 presents the hydrogeologic properties assigned for each formation (Wainwright et al., 2013). These properties are based on site characterization data available from oil and gas exploration and groundwater development in the area. Two Quaternary faults, the Pond-Poso-Creek (PPC) fault zone and the New Hope fault, and the older Greeley fault are mapped at the surface (Wagoner, 2009) (Fig. 2). Here, we focus on the geomechanical stability of the PPC fault during a hypothetical carbon sequestration project. We have selected the PPC fault because this fault bounds the sequestration site and is mapped as a Quaternary fault. The PPC fault consists of three segments A-B, B-C and C-D with strikes N140°E, N095°E and N132°E, respectively (Fig. 2). The orientation of S_{Hmax} is close to N21°E ± 7° (Chanchani et al., 2003), and the stress state prior to reservoir pressure depletion was estimated to be a reverse/strike-slip faulting regime (with S_v = 25 MPa, S_{hmin} = 26 MPa and $S_{Hmax} \geq$ 54 MPa) at the western side of the study area (Chanchani et al., 2003).

3. Numerical simulation

The numerical simulations were conducted with TOUGH-FLAC (Rutqvist, 2011) based on sequentially coupling the TOUGH2 multiphase flow simulator (Pruess et al., 2012) with the FLAC3D geomechanics simulator (ITASCA, 2011). The sequential one-way coupling approach used here involves coupling of multi-scale model domains and is fully described in Jeanne et al. (2016). The main idea is to use the flexibility provided by this hydraulic and mechanical coupling approach, using different numerical grids for each sub-problem. A basin-scale model is used to accurately model the effects of the complex geometries of reservoir-bounding faults and calculate the pressure distribution within a wide damage zone (Fig. 2a). A sufficiently fine-grid resolution is used to represent a thin fault core (Fig. 2b) to be able to mechanistically to calculate the evolution of seismicity and seismic moment magnitudes.

3.1. Fluid flow simulations

The 3D basin-scale reservoir model extends to a depth of 3.5 km, and laterally 84 km in the eastern and 122 km in the northern direction (Wainwright et al., 2013; Zhou and Birkholzer, 2011). Eleven formations from the crystalline base rock to the top shallow aquifer are represented, as are the Greeley, PPC and New Hope fault zones (Fig. 2a). These faults are vertical in the fluid flow simulation and 500 m wide. We consider a hypothetical scenario in which two fault zones trending northeast-southwest are present resulting in a compartmentalization of the targeted reservoir (faults in blue in Fig. 2a). The faults are impermeable except the PPC fault (in red in Fig. 2a). This fault has an impermeable fault core and a permeability within the damage zone (along both strike and dip) two orders of magnitude higher than the adjacent host rock (Table 1). Finally, the porosity of the PPC fault is assumed to vary according to the initial properties of the adjacent host rock sedimentary layers (Jeanne et al., 2012).

We simulate a CO_2 injection into the deep Vedder formation in the center of the domain (at 7.2 km from the PPC fault) at a rate of 20 million metric tons of CO_2 per year for a period of 50 years. The multiphase basin-scale flow simulation is performed with the parallel version of the TOUGH2 multiphase flow simulator, i.e. TOUGH2-MP (Zhang et al., 2008) with the ECO2N module to simulate injection and migration of supercritical CO_2 in the brine-filled reservoir (salinity of 15%). The ECO2N module describes the thermodynamics and thermophysical properties of H_2O-NaCl-CO_2 mixtures, including phase transitions and dissolutions (Pruess, 2005). We set the initial conditions assuming linear pore pressure and temperature gradients (9.81 MPa/km and 25 °C/km, respectively), with constant hydraulic boundary conditions (i.e., open to fluid flow) on the model vertical boundaries and on

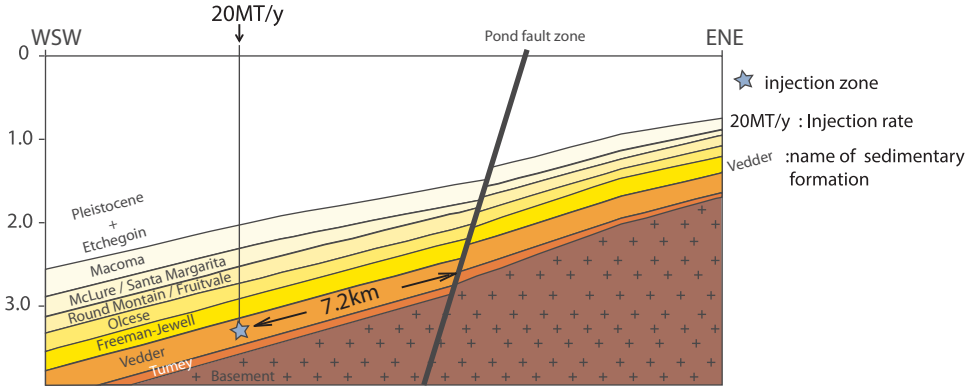

Fig. 1. Geological cross section the Southern San Joaquin Basin (from Wagoner, 2009).

Table 1
Hydrogeologic properties assigned to each formation outside and within the PPC fault zone. Kv and Kh are the vertical and horizontal permeability, respectively, β_p is pore compressibility, α is the van Genuchten parameter for entry capillary pressure, and m is the van Genuchten parameter for pore-size distribution (van Genuchten, 1980).

	Formations		Pond-Poso-Creek fault		β_p (10^{-10} Pa^{-1})	α (10^{-5} Pa^{-1})	m (–)
	permeability Kv = Kh (m^2)	porosity	Permeability Kv = Kh (m^2)	porosity			
Pleistocene	3.00E-12	0.35	3.00E-10	0.16	15.5	5	0.457
Etchegoin	1.20E-12	0.32	1.20E-10	0.16	15.5	5	0.457
Macoma	1.90E-12	0.31	1.90E-10	0.16	10.5	5	0.457
Santa Margarita	2.00E-12	0.28	2.00E-10	0.14	14.5	0.42	0.457
Round Mountain	2.00E-18	0.02	4.00E-16	0.1	4.9	5	0.457
Olcese	1.70E-13	0.34	1.70E-11	0.17	14.5	0.42	0.457
Freeman	2.00E-18	0.02	4.00E-16	0.1	4.9	13	0.457
Vedder sand	5.56E-13	0.28	3.03E-11	0.13	14.5	0.42	0.457
Vedder Shale	1.00E-16	0.1	2.00E-14	0.15	14.5	0.42	0.457
Tumey	2.00E-18	0.07	2.00E-16	0.14	22.7	0.5	0.457

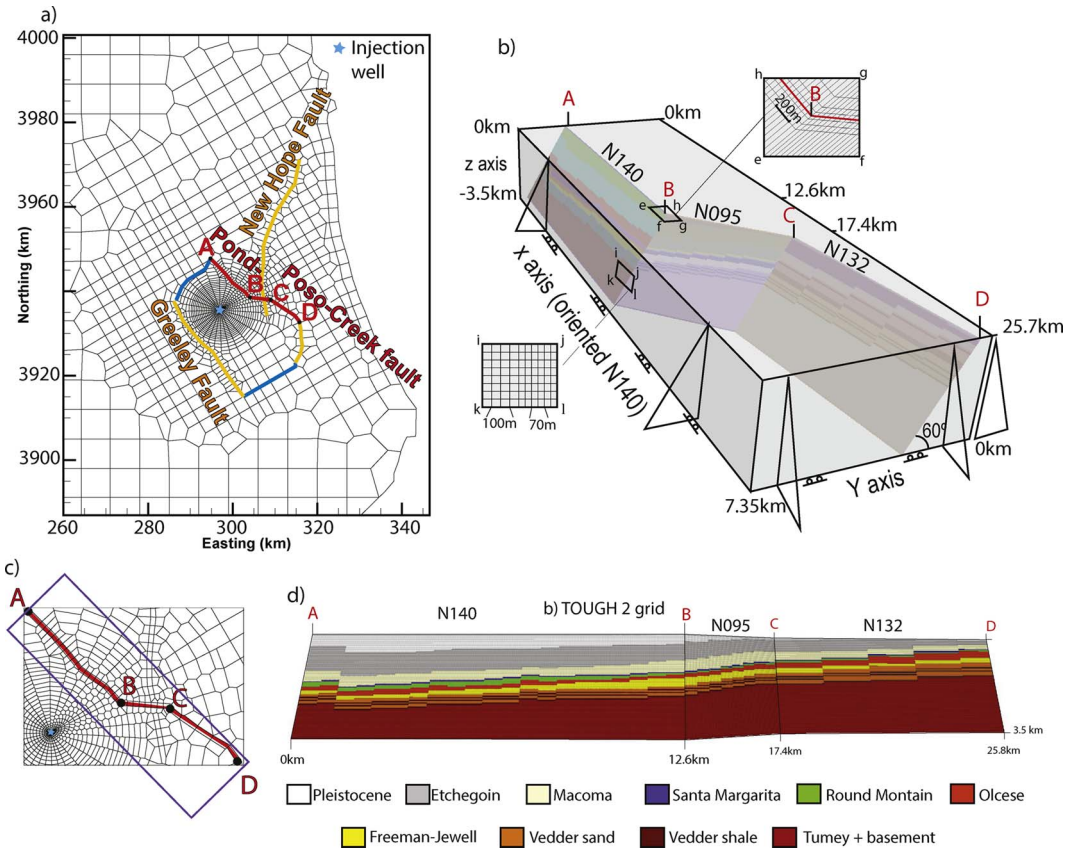

Fig. 2. (a) Basin-scale reservoir model used in the fluid flow simulation. (b) FLAC3D grid used in the geomechanical simulation. (c) Details of fluid flow grid discretization towards the center of the model (the blue rectangle in 2c represents the boundaries of the geomechanical model) and (d) along the fault. (For interpretation of the references to colour in this figure legend, the reader is referred to the web version of this article.)

the top boundary (temperature and pressure at the top layer are 20° C and atmospheric pressure, respectively). The simulation is isothermal, because we assume that CO_2 is injected under thermal equilibrium with the storage formation.

3.2. Geomechanical stability of the PPC fault

We use the numerical simulator TOUGH-FLAC to investigate fault reactivation and the associated seismicity during CO_2 injection. The pressure and CO_2 distribution within the damage zone of the PPC fault (1466 elements) are extracted from the basin scale reservoir model every 7 days during 50 years of injection. These data are linearly interpolated cell by cell to a more refined mesh on the faults (41,280 rectangular elements of 50 m × 0.10 m × 50 m) used to evaluate the geomechanical stability of the PPC fault core every week during 50 years of injection with the numerical simulator TOUGH-FLAC. In this approach rupture along the fault has not influence on pressure evolution. This one-way hydromechanical coupling could underestimate pore pressure diffusion and volumetric strains in the fault compared to a two-way hydromechanical coupling. This implies that eventually different seismic activity would occur if a two-way coupling technique were to be employed. Also, the long-term fluid-rock interaction could occur along the fault core, possibly altering the lithology of fault core (Ellis et al., 2013; Kohli and Zoback, 2013; Fang et al., 2017; Wang et al., 2017), thus changing the fault friction properties and so affect the fault stability and the associated seismic activity. However, given the relatively small size of the CO_2 plume along the fault in comparison to the pressurized zone, this additional effect would be confined along the fault in closer proximity to the injection well and so we did not consider geochemical reaction in our model.

The FLAC3D grid extends laterally about 25 km by 7.5 km and is 3.5 km deep. It is discretized into 371,520 (=41,280 × 9) elements (Fig. 2b). Pressure and CO_2 distribution are only updated along the fault core during the TOUGH-FLAC simulation. No fluid flow occurs between the fault and the surrounding host rock, which also means that poroelastic stress changes that could occur in the surrounding rock are considered negligible. The laterally extended part of the 3D geomechanical model is needed to initialize and apply the in situ stress state and to allow the fault to slip when rupture nucleates. This part has a Young's modulus of 15 GPa and a Poisson's ratio equal to 0.25. We simulated the case of a stress regime in which the maximum principal compressive stress $\sigma_1 = S_{Hmax}$, intermediate stress $\sigma_2 = 1.1 \times S_v$, and the least compressive principal stress, $\sigma_3 = S_v = \rho g h$, with ρ the rock density, g the acceleration of gravity and h the depth. The ratio $R = \sigma'_1/\sigma'_3 = (\sigma_1 - \alpha P_f)/(\sigma_3 - \alpha P_f)$ is set equal to 2.30 where P_f is the initial hydrostatic pore fluid pressure and $\alpha = 1$ the Biot coefficient, and S_{Hmax} is oriented N10°. The stress tensor is applied on the vertical boundaries and follows the lithostatic gradient. On the top boundary, the ground surface is free to move.

We consider a finite thickness fault (0.1 m) and use a ubiquitous joint model with a Mohr-Coulomb elasto-plastic failure criterion and with strain-hardening and strain-softening frictional laws. The ubiquitous joint model considers the presence of a weakness plane that is oriented N140, N095 and N132 along the fault segment A-B, B-C and C-D, respectively (Fig. 2b). To assess how the representation of the coefficient of friction and the friction law could affect the prediction of the geomechanical stability of the PPC fault during CO_2 injection, we conduct nine simulations in which the distributions of friction parameters along the PPC fault are different. Specifically, we change μ_s and the amount of hardening (μ_{dHard}) and softening (μ_{dSoft}) during rupture.

- μ_s is either homogeneously distributed ($\mu_s = 0.6$) (Fig. 3a), uniformly distributed ($0.6 \leq \mu_s \leq 0.7$) (Fig. 3b), or uniformly distributed over ranges depending on host rock lithology: ($0.5 \leq \mu_s \leq 0.6$ in clay layers, and $0.6 \leq \mu_s \leq 0.7$ in sandstone and crystalline rock) (Fig. 3c).
- $\mu_{d\text{-}Hard}$ is either uniformly distributed ($\mu_s \leq \mu_{d\text{-}Hard} \leq \mu_s + x$, with x ranging from 0 to 0.1) (Fig. 4a and d), or a homogeneous friction coefficient depending on the host rock lithology ($\mu_{d\text{-}Hard} = 0.65$ and 0.75 in clay layers and crystalline rock, respectively) (Fig. 4b–f).
- $\mu_{d\text{-}Soft}$ is either homogeneously distributed ($\mu_{d\text{-}Soft} = 0.4$) or uniformly distributed between μ_s and 0.4.

μ_s evolves first towards $\mu_{d\text{-}Hard}$ when the plastic shear strain on the fault core reaches a critical value of 1×10^{-5} and then to $\mu_{d\text{-}Soft}$ when the strain reaches 2×10^{-5}. The drop in the coefficient of friction and the strain threshold were chosen to simulate a brittle (slip weakening) fault rheology that results in substantial and distinct seismic slips across areas of fault rupture. μ_s ranging from 0.6 to 0.7 is in agreement with average values at the depth considered, while the lowest value for $\mu_{d\text{-}Soft}$ ($\mu_{d\text{-}Soft} = 0.4$) is calibrated to avoid unrealistic run-away rupture after reactivation. The tests are summarized in Table 2 and illustrated in Fig. 4. Results are compared with a simulation presented in Jeanne et al. (2016), where $\mu_s = 0.6$ and $\mu_{dSoft} = 0.4$ (no hardening part was simulated; see the purple curve on Fig. 4d).

3.3. Assessment of the induced seismic activity

One geomechanical simulation is performed every week during the 50-year period of injection. To estimate the seismic activity we compare each geomechanical simulation with the previous one. A seismic event during a simulation corresponds to shear failure (rupture) of cells within the fault plane that have not been activated previously (plastic shear strain equal to zero). One or several seismic events can occur depending on the Euclidian distance between the cells that fail. For example, if failure occurs on two adjacent cells (Euclidian distance smaller than $(50^2 + 50^2)^{0.5\ m} = 71$ m), we consider that a rupture that nucleates on one patch and propagates to the second one, representing a single seismic event. Conversely, failures that occur on two cells that are not in contact (Euclidian distance > 71m) are considered as two separate events. Using this approach, the seismic activity is related only to the propagation of rupture along the fault in areas that were previously stable. Ruptures occurring in a previously active area are not associated with changes in friction coefficient (Fig. 4) allowing sudden and distinct seismic slips so in our simulation the fault creeps and we consider these deformations to be aseismic. Also, because we look at the rupture distribution only on a weekly basis, there is a possibility that what appears as one event is in reality a cluster of smaller events, which can lead to overestimation of event magnitudes and underestimation of the number of events. We also assume that there is no seismic activity in the shallow region (above – 500 m), since ruptures that nucleate within this low stress region are inhibited from propagating (Das and Scholz, 1983), corresponding to a displacement hardening friction law.

For each event we calculate the average slip, the area of rupture, the average changes in fluid pressure responsible for the event, the seismic moment and moment magnitude, and the normal and shear stress after rupture. The fault core is represented with multiple solid elements, when failure occurs these elements are dislocated. We used the node displacements in the x, y and z directions occurring during the dislocation to estimate the slip vector. In case of rupture along several elements, a slip vector is calculated for each of these elements and an average slip is calculated. The static seismic moment of an event is given by (e.g., Kanamori and Brodsky, 2004)

$$M_o = GAd \tag{1}$$

where G is the shear modulus (2 GPa in our study), A the rupture area and d the slip. Moment magnitude is estimated using the equation (Hanks and Kanamori, 1979):

$$M_w = \frac{2}{3} \times [\log_{10}(M_o) - 16.1] \tag{2}$$

where M_0 is in dyne-cm.

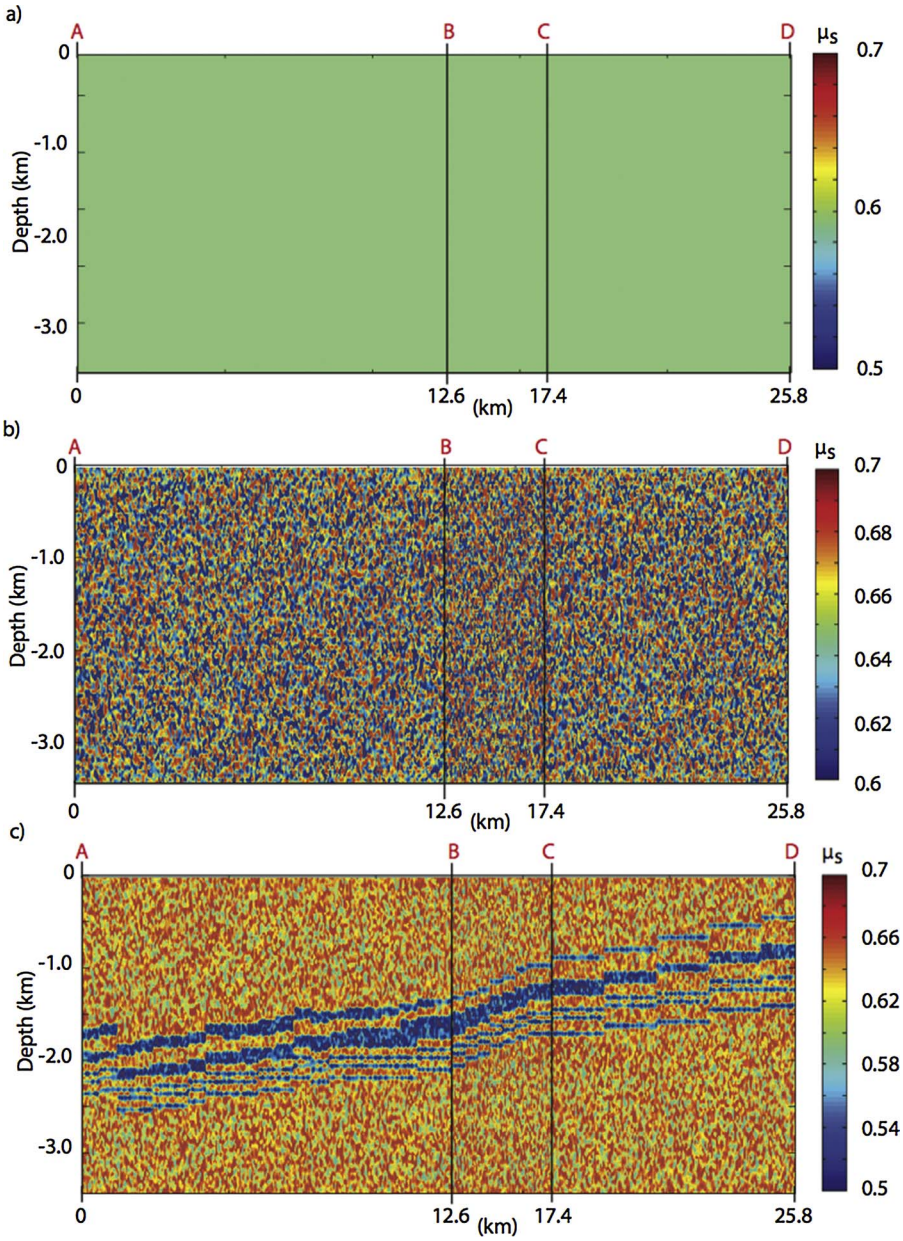

Fig. 3. Distribution of the coefficient of static friction in the three base case scenarios, with μ_s: (a) homogeneously distributed, (b) uniformly distributed and (c) uniformly distributed according to the host rock lithology.

The normal σ (MPa) and shear stress τ (MPa) acting on the fault are (Jaeger et al., 2007):

$$\sigma = l^2\sigma_1 + m^2\sigma_2 + n^2\sigma_3 \quad (3)$$

$$\tau = [(\sigma_1 - \sigma_2)^2 l^2 m^2 + (\sigma_2 - \sigma_3)^2 m^2 n^2 + (\sigma_1 - \sigma_3)^2 l^2 n^2]^{0.5} \quad (4)$$

where *l*, *m* and *n* are the direction cosines normal to the fault plane with respect to the principal stress axes, σ_1, σ_2 and σ_3, respectively.

For each seismic event, we characterize the properties of the frictional law for the rupture area. We extract the lowest and highest values of μ_s, $\mu_{d\text{-}Hard}$ and $\mu_{d\text{-}Soft}$ and calculate the highest and lowest difference between μ_s and $\mu_{d\text{-}Hard}$ ($\Delta max\mu_{sH}$ and $\Delta min\mu_{sH}$, respectively) and between $\mu_{d\text{-}Hard}$ and $\mu_{d\text{-}Soft}$ ($\Delta max\text{-}\mu_{HS}$ and $\Delta min\text{-}\mu_{HS}$, respectively) (Fig. 5a). We also calculate the average increase in friction during the hardening phase and the average drop in friction during the softening phase. For this reason, we calculate an average μ_s, $\mu_{d\text{-}Hard}$ and $\mu_{d\text{-}Soft}$ (annoted av-μ_s, av-$\mu_{d\text{-}Hard}$ and av-$\mu_{d\text{-}Soft}$, respectively), and finally we calculate the differences between av-μ_s and av-$\mu_{d\text{-}Hard}$ (av-$\Delta\mu_{sH}$) and between av-$\mu_{d\text{-}Hard}$ and av-$\mu_{d\text{-}Soft}$ (av-$\Delta\mu_{HS}$) (Fig. 5b).

At the end of 50 years of injection and once a seismic catalog is created, we look at the empirical relation between the frequencies of occurrence and magnitudes of the simulated induced events as described by Eq. (5) (Gutenberg and Richter, 1954).

$$\log_{10} N = a - bM \quad (5)$$

where N is the total number of earthquakes per unit time with magnitudes ≥M. The a-value describes the seismic productivity, which depends on the area and time period of investigation, and the b-value describes the earthquake frequency-magnitude distribution.

4. Results

4.1. Pressure distribution along the PPC fault

Fig. 6 shows the pore pressure variations along the PPC fault at the end of the injection at 50 years. The pore pressure mostly increases where the targeted reservoir intersects the PPC fault. Indeed, despite that the fault permeability across the caprock being two orders of magnitude higher than the adjacent host caprock permeability, changes

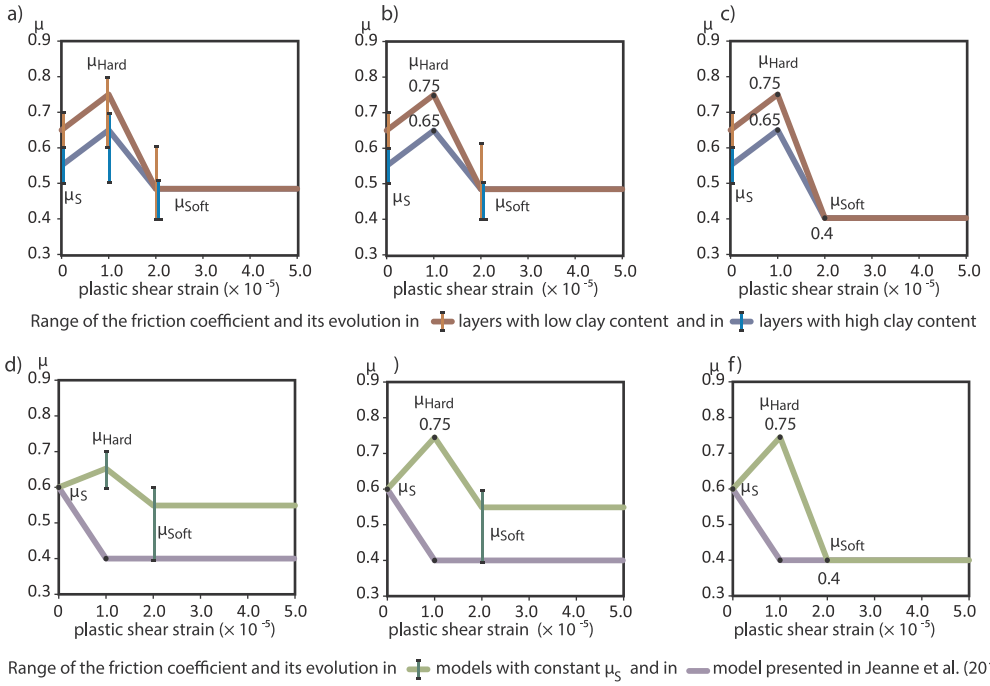

Fig. 4. Illustrations of strain-hardening/softening frictional laws described in Table 2 and used in Flac3D. The red line in (a to c) represents how μ_d could evolve in case of a uniform distribution of μ_s (Fig. 3b). The blue line represents how μ_d could evolve in layer with high clay content when μ_s is uniformly distributed according to the host rock lithology (Fig. 3c). Finally, the green line in (d to f) represents how μ_d could evolve when μ_s is homogeneously distributed (Fig. 3a). (For interpretation of the references to colour in this figure legend, the reader is referred to the web version of this article.)

Table 2
Range of coefficient of static and dynamic friction used in the geomechanical simulation. The coefficient values used for the geological layers with high clay content are in blue. (For interpretation of the references to colour in this table legend, the reader is referred to the web version of this article.)

	μ_s	$\mu_{d\text{-Hard}}$	$\mu_{d\ Soft}$
test1	[0.5-0.6] / [0.6-0.7]	[0.5-0.7] / [0.6-0.8]	[0.4-0.6] / [0.4-0.7]
test2	[0.5-0.6] / [0.6-0.7]	0.65 / 0.75	[0.4-0.6] / [0.4-0.7]
test3	[0.5-0.6] / [0.6-0.7]	0.65 / 0.75	0.4 / 0.4
test4	[0.6-0.7]	[0.6-0.8]	[0.4-0.7]
test5	[0.6-0.7]	0.75	[0.4-0.7]
test6	[0.6-0.7]	0.75	0.4
test7	0.6	[0.6-0.7]	[0.4-0.6]
test8	0.6	0.7	[0.4-0.6]
test9	0.6	0.7	0.4

in pore pressure within the rock formations above the caprock are very limited. The homogeneous pore pressure distribution along the fault over time is due to the high injection rate into a compartmentalized and (≈350 m thick) reservoir, and to the high permeability along its strike and dip, which allows for rapid pore pressure diffusion. Fig. 6b also shows that the CO_2 at the end of injection is confined within the targeted reservoir and no major leaks occur along the fault during the first 50 years.

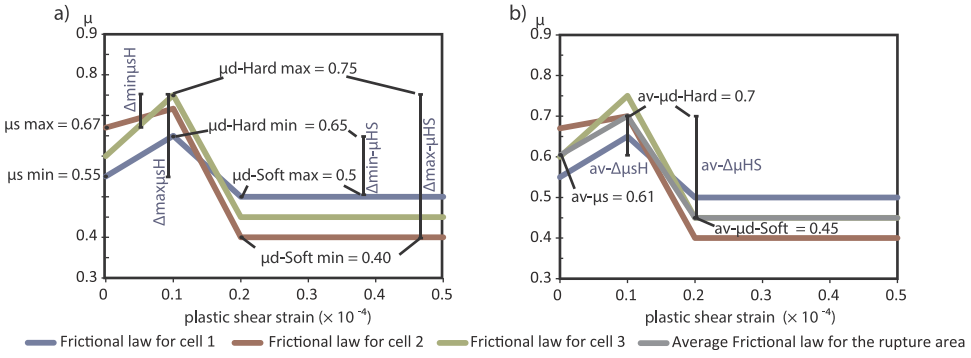

Fig. 5. Frictional attributes calculated from (a) the minimum and maximum value of μ_s, $\mu_{d\text{-Hard}}$ and $\mu_{d\text{-Soft}}$ and (b) from the average values of μ_s, $\mu_{d\text{-Hard}}$ and $\mu_{d\text{-Soft}}$. Example of a single event propagating into three adjacent cells having three different frictional laws (blue, red and green curves). These three cells could have the same lithology. (For interpretation of the references to colour in this figure legend, the reader is referred to the web version of this article.)

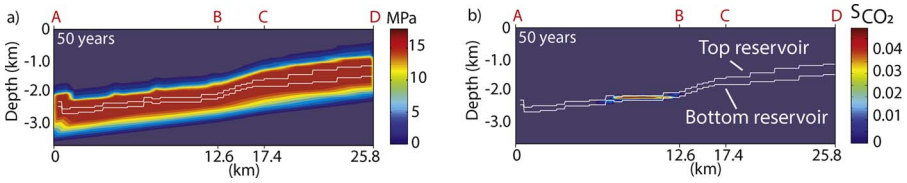

Fig. 6. (a) Pressure distribution along the PPC fault and (b) CO_2 saturation after 50 years of injection.

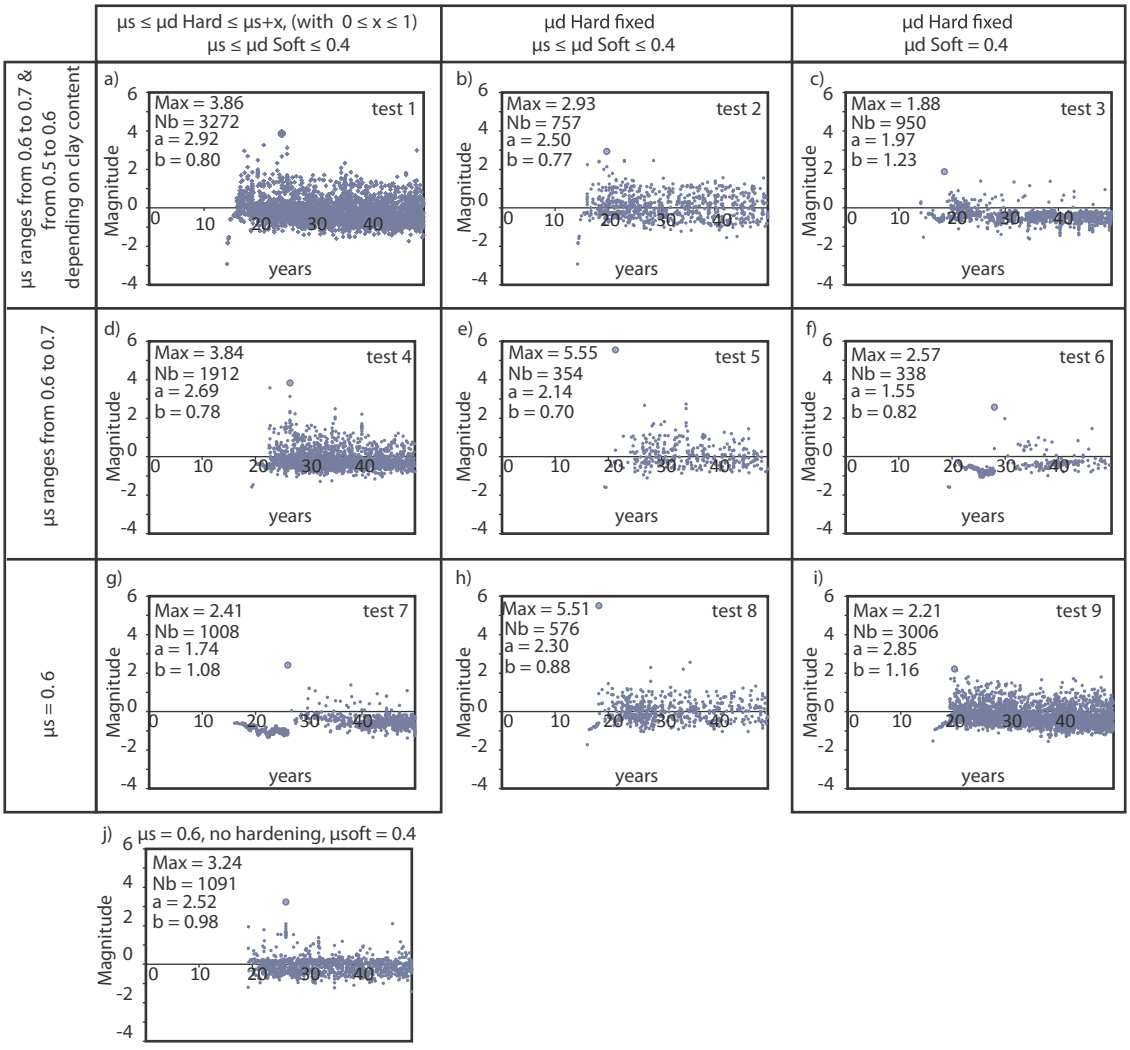

Fig. 7. Seismic catalogs comprising nine scenarios calculated in this study (tests a to i and one from Jeanne et al. (2016) (test j).

4.2. Geomechanical stability and induced seismic activity

Fig. 7 shows ten seismic catalogs: nine calculated in this study and one from Jeanne et al. (2016). We observed a large difference in the calculated maximum seismic magnitude (ranging from 1.88 to 5.55) and in the total number of seismic events per simulation (from 338 to 3272). To investigate the causes of these differences, the simulation results are analyzed using principal component analysis (PCA) (Jolliffe, 2002). A PCA is a statistical technique used to find correlations between a set of variables and to reveal the underlying structure of the data set. Here, two PCAs were performed in order to extract the main trends and correlations between the seismic response and the frictional properties.

The first factorial analysis is performed on a composite seismic catalog compiled from the nine catalogs calculated in this study. There are 12173 seismic events in total and each event is characterized by its area of rupture (A), the average slip (Slip), the average change in fluid pressure inducing the seismic event (ΔP), the magnitude (M_w), the normal (σ) and shear stresses (τ) after rupture, the highest and lowest difference between μ_s and $\mu_{d\text{-}Hard}$ ($\Delta max\mu_{sH}$ and $\Delta min\mu_{sH}$, respectively) and between $\mu_{d\text{-}Hard}$ and $\mu_{d\text{-}Soft}$ ($\Delta max\text{-}\mu_{HS}$ and $\Delta min\text{-}\mu_{HS}$, respectively), the differences between the average μ_s, and the average $\mu_{d\text{-}Hard}$ (av-$\Delta\mu_{sH}$) and between the average $\mu_{d\text{-}Hard}$ and the average $\mu_{d\text{-}Soft}$ (av-$\Delta\mu_{HS}$). The PCA reveals three main correlations (or three principal components) explaining 70% of the underlying structure in the seismic catalogs (Table 3).

- Axis 1 is determined by (i) the relation between av-$\Delta\mu_{sH}$ and av-$\Delta\mu_{HS}$ used to create the input file and by (ii) a relation between the average values between $\mu_{d\text{-}Hard}$ and $\mu_{d\text{-}Soft}$ (av-$\Delta\mu_{HS}$) and the highest and lowest differences between $\mu_{d\text{-}Hard}$ and $\mu_{d\text{-}Soft}$ ($\Delta max\text{-}\mu_{HS}$ and $\Delta min\text{-}\mu_{HS}$, respectively). For these reasons no attention is given to this axis.
- Axis 2 highlights the positive correlation between the change in pore pressure, the normal and shear stress acting on the fault and the

Table 3
Results of the first factorial analysis, with the red cells showing the variables with a strong correlation along each axis, the percentage of explained variance (%), the accumulated percentage of explained variance (Tot%) and the significance of each axis in blue. (For interpretation of the references to colour in this table legend, the reader is referred to the web version of this article.)

Attribute	Axis_1		Axis_2		Axis_3	
-	Corr.	% (Tot. %)	Corr.	% (Tot. %)	Corr.	% (Tot. %)
Δmin-μ_{HS}	0.92	85 % (85 %)	-0.06	0 % (85 %)	0.05	0 % (85 %)
av-$\Delta\mu_{HS}$	0.89	79 % (79 %)	-0.04	0 % (79 %)	0.07	0 % (79 %)
av-$\Delta\mu_{sH}$	0.78	61 % (61 %)	-0.08	1 % (62 %)	0.26	7 % (68 %)
Δmax-μ_{HS}	0.75	56 % (56 %)	0.05	0 % (57 %)	-0.59	35 % (92 %)
ΔP	0.06	0 % (0 %)	0.90	81 % (81 %)	0.05	0 % (82 %)
A	0.06	0 % (0 %)	0.86	74 % (75 %)	0.04	0 % (75 %)
σ	0.05	0 % (0 %)	0.81	66 % (66 %)	0.21	4 % (70 %)
τ	0.05	0 % (0 %)	0.81	66 % (66 %)	0.22	5 % (70 %)
Δminμ_sH	0.41	16 % (16 %)	-0.15	2 % (19 %)	0.84	70 % (88 %)
Δmaxμ_sH	0.42	18 % (18 %)	0.09	1 % (19 %)	-0.73	54 % (73 %)
M_w	-0.17	3 % (3 %)	0.26	7 % (10 %)	-0.51	26 % (36 %)
Slip	0.01	0 % (0 %)	0.34	11 % (11 %)	-0.12	2 % (13 %)
Var. Expl.	3.20	27 % (27 %)	3.10	26 % (52 %)	2.03	17 % (69 %)

surface of rupture. This means that for higher ambient stress higher changes in pore pressure is needed to induce a seismic event and a larger rupture occurs.

- Axis 3 shows a positive correlation between the magnitudes, Δmaxμ_{sH} and Δmax-μ_{HS}, and a negative correlation with Δminμ_{sH}.

We also observe that the magnitudes of the calculated seismic events are not correlated with the average friction properties on the rupture areas, but with the extreme values of the coefficient of friction (lowest and highest) within the rupture area. Indeed, higher magnitudes occur when the difference between the lowest μ_s and the highest $\mu_{d\text{-}Hard}$ is large (high ΔmaxμsH and low ΔminμsH) and when the difference between $\mu_{d\text{-}Hard}$ and $\mu_{d\text{-}Soft}$ is large. These extreme values control the amount of stress accumulated during the hardening part and the amount of stress released during the softening part.

The second factorial analysis is performed on results obtained from the nine simulations done during this study and the one from Jeanne et al. (2016). The seismic attributes tested in the second analysis are summarized in Table 4. These are: the time between the beginning of the injection and the nucleation of the first seismic event (Time), maximum simulated magnitude (max M_w), total number of seismic events per simulation (Nb), total activated area of the fault at the end of the simulation (A_{Tot}), total seismic moment released during injection (M_{Tot}), the a and b-values of the frequency-magnitude distribution, the highest and lowest μ_s (max-μ_s and min-μ_s), $\mu_{d\text{-}Hard}$ (max-$\mu_{d\text{-}Hard}$ and min-$\mu_{d\text{-}Hard}$) and $\mu_{d\text{-}Soft}$ (max-$\mu_{d\text{-}Soft}$ and min-$\mu_{d\text{-}Soft}$) present along the fault plane. Table 5 presents the results of this component analysis.

Three axes (or three principal components) are needed to explain 73% of the underlying structure in the dataset (axes 1, 2 and 3, explain ~30%, ~24% and ~19%, respectively). Axis 1 is related to the correlation between the variables min-$\mu_{d\text{-}Hard}$, min-μ_s, and Time, which are all negatively correlated to the variables max-$\mu_{d\text{-}Soft}$, Nb and a-value. Axis 2 is driven by the correlation between max M_w, M_{Tot}, max-μ_s and max-$\mu_{d\text{-}Hard}$, which are all negatively correlated to the b-value. These two axes show the influence of the friction coefficient on the stress accumulation before the softening part and how it affects the seismic activity. Axis 1 shows that faults having a frictional law characterized by an initial low coefficient of static friction and a small hardening part (min-$\mu_{d\text{-}Hard}$ and min-μ_s) prevent substantial strengthening stress accumulation before rupture and are easier to reactivate (Time). The small drop in friction during the softening part (high max-$\mu_{d\text{-}Soft}$) also prevents the stress from being fully released and rupture keeps occurring. Therefore, the seismic activity associated with the reactivation of such a fault is characterized by a large number of seismic events (high Nb and a-value) of lower magnitude. This can be seen by comparing the seismic catalogs obtained during tests 2, 5 and 8 (Fig. 7b, e and h), by considering lower coefficients of static friction and lower values of $\mu_{d\text{-}Hard}$ in the caprock, the number of seismic events is almost increased by a

Table 4
Seismic attributes obtained from the nine geomechanical simulations, which are the time between the beginning of the injection and the nucleation of the first seismic event (Time), maximum simulated magnitude (max M_w), total number of seismic events per simulation (Nb), total activated area of the fault at the end of the simulation (A_{Tot}), total seismic moment released during injection (M_{Tot}), the a- and b-value of the frequency-magnitude distribution, the highest and lowest μ_s (max-μ_s and min-μ_s), $\mu_{d\text{-}Hard}$ (max-$\mu_{d\text{-}Hard}$ and min-$\mu_{d\text{-}Hard}$) and $\mu_{d\text{-}Soft}$ (max-$\mu_{d\text{-}Soft}$ and min-$\mu_{d\text{-}Soft}$) present along the fault plane.

Time (Year)	max Mw	Nb	A_{Tot} (m^2)	M_{Tot}	a	b	μ_s		$\mu_{d\text{-}Hard}$		$\mu_{d\text{-}Soft}$	
							min	max	min	max	min	max
14.21	3.86	3272	2.2E+11	1.1E+22	2.92	0.80	0.5	0.7	0.5	0.8	0.4	0.7
14.21	2.93	757	3.6E+11	7.5E+20	2.50	0.77	0.5	0.7	0.5	0.8	0.4	0.4
14.13	1.88	950	2.0E+11	2.0E+19	1.98	1.24	0.5	0.7	0.65	0.75	0.4	0.4
19.31	3.84	1912	1.2E+11	1.1E+22	2.69	0.78	0.5	0.7	0.6	0.8	0.4	0.7
19.31	5.55	354	1.6E+11	2.6E+24	2.14	0.70	0.5	0.7	0.6	0.8	0.4	0.4
19.31	2.57	338	1.9E+11	1.1E+20	1.55	0.82	0.6	0.7	0.75	0.75	0.4	0.4
16.06	2.21	3006	2.4E+11	1.9E+20	2.85	1.16	0.6	0.6	0.6	0.7	0.4	0.6
16.06	2.41	1008	2.1E+11	6.0E+19	1.74	1.08	0.6	0.6	0.75	0.75	0.4	0.4
16.06	5.51	576	3.8E+11	2.3E+24	2.30	0.88	0.6	0.6	0.6	0.75	0.4	0.4
19.23	3.24	1091	3.0E+11	1.0E+21	2.52	0.98	0.6	0.6	0.6	0.6	0.4	0.4

Table 5
Results of the second factorial analysis, with the red cells showing the variables with a strong correlation along each axis, the percentage of explained variance (%) the accumulated percentage of explained variance (Tot%), and the significance of each axis in blue. (For interpretation of the references to colour in this table legend, the reader is referred to the web version of this article.)

Attribute	Axis_1		Axis_2		Axis_3	
-	Corr.	% (Tot. %)	Corr.	% (Tot. %)	Corr.	% (Tot. %)
Nb	0.79	*63 % (63 %)*	0.26	*7 % (70 %)*	-0.14	*2 % (72 %)*
a-value	0.78	*61 % (61 %)*	-0.07	*0 % (61 %)*	-0.52	*27 % (89 %)*
max-$\mu_{d\text{-Soft}}$	0.77	*60 % (60 %)*	-0.09	*1 % (60 %)*	0.04	*0 % (61 %)*
min-$\mu_{d\text{-Hard}}$	-0.75	*57 % (57 %)*	0.31	*10 % (66 %)*	0.47	*22 % (89 %)*
min-μ_s	-0.67	*45 % (45 %)*	-0.13	*2 % (47 %)*	-0.21	*4 % (51 %)*
Time	-0.55	*30 % (30 %)*	-0.41	*16 % (46 %)*	0.07	*1 % (47 %)*
b-value	-0.10	*1 % (1 %)*	0.89	*80 % (81 %)*	0.00	*0 % (81 %)*
max M_w	-0.10	*1 % (1 %)*	-0.85	*72 % (73 %)*	-0.45	*21 % (93 %)*
M_{Tot}	-0.38	*14 % (14 %)*	-0.69	*47 % (62 %)*	-0.39	*15 % (76 %)*
max-$\mu_{d\text{-Hard}}$	0.43	*18 % (18 %)*	-0.52	*27 % (45 %)*	0.59	*35 % (81 %)*
A_{Tot}	-0.05	*0 % (0 %)*	0.20	*4 % (4 %)*	-0.74	*54 % (58 %)*
max-μ_s	0.38	*15 % (15 %)*	-0.49	*24 % (39 %)*	0.67	*46 % (85 %)*
min-$\mu_{d\text{-Soft}}$	0.00	*0 % (0 %)*	0.00	*0 % (0 %)*	0.00	*0 % (0 %)*
Var. Expl.	3.64	*30 % (30 %)*	2.90	*24 % (54 %)*	2.27	*19 % (73 %)*

factor two (from 354 in test 5 to 757 in test 2) and the highest magnitude of the induced event almost halved (from 5.55 in test 5 to 2.93 in test 2).

Inversely, axis 2 shows that a frictional behavior characterized by a high initial coefficient of static friction and a more significant hardening phase favors stress accumulation and leads to induced seismic events of higher magnitude and low b-values. Axis 3 shows that with a smaller number of seismic events the total rupture area is smaller.

5. Summary and conclusions

This study is based on a hypothetical, industrial-scale carbon sequestration project in the Southern San Joaquin Basin in California. Our goals were to assess the geomechanical stability of the Quaternary Pond-Poso-Creek fault zone mapped at the surface and to investigate how the uncertainties related to friction properties could influence our results. The friction properties of a fault are normal stress and roughness dependent (Fang et al., 2016; Mair and Marone, 1999) and also depend on the fault's seismic history (number of seismic events, magnitude, etc.). Therefore, a complex distribution of fault parameters can be expected, more like the rupture patch distribution resulting from previous slip events. In this paper, we carried out simulations with distributions of fault frictional parameters ranging from a very simple to more complex distribution of the fault friction parameter, but with a uniform distribution of the static coefficient of friction according to the host rock lithology. The more complex representation of fault parameters is still not well adapted to represent a patch distribution but interesting observations can still be made. The main findings of our study are:

- The effect of the uncertainty related to (i) the distributions of the coefficients of friction along the fault and (ii) to the constitutive parameters of the frictional law have a strong effect on the prediction of the seismic activity (maximum magnitude, number of seismic events and a- and b-values).
- The seismic activity is strongly dependent on the amount of stress accumulated along the fault before rupture. This depends on the fault frictional properties, but there are large uncertainties on those values and further laboratory- and field-scale research is required to reduce them. Here, we show that the amount of stress does not depend on the average frictional properties of the rupture areas, but on the lowest and highest values of the static and dynamic coefficients of friction present along the rupture area. These results could have important implications when assessing fault stability based on frictional properties obtained from laboratory tests. The extreme values of μ_s, $\mu_{d\text{-Hard}}$ and $\mu_{d\text{-Soft}}$ must be considered, not an average value.
- Argillaceous caprock and low values of the coefficient of static friction can prevent the occurrence of high magnitude seismic events. Indeed, a low coefficient of static friction prevents large stress accumulation before rupture. However, the seismic activity associated with the reactivation of such a fault will be characterized by a large number of seismic events of lower magnitude.

Acknowledgements

This work was funded by the Assistant Secretary for Fossil Energy, National Energy Technology Laboratory, National Risk Assessment Partnership, of the U.S. Department of Energy under Contract No. DEAC02-05CH11231. A.P. Rinaldi is currently funded by Swiss National Science Foundation Ambizione Energy grant (PZENP2_160555), and the three anonymous reviewers were also honored by improving the manuscript's quality.

References

Amontons, 1699. Les loi de la friction.
Bachmann, C., Wiemer, S., Goertz-Allmann, B., Woessner, J., 2012. Influence of pore pressure on the size distribution of induced earthquakes. Geophys. Res. Lett. 39, L09302. http://dx.doi.org/10.1029/2012GL051480.
Birkholzer, J.T., Zhou, Q., Cortis, A., Finsterle, S., 2011. A sensitivity study on regional pressure buildup from large-scale CO_2 storage projects. Energy Procedia 4, 4371–4378.
Byerlee, J.D., 1978. Friction of rocks. Pure Appl. Geophys. 116, 615–626.
Cappa, F., Rutqvist, J., 2011. Modeling of coupled deformation and permeability evolution during fault reactivation induced by deep underground injection of CO_2. Int. J. Greenh. Gas Control 5, 336–346.
Catalli, F., Rinaldi, A.P., Gischig, V., Nespoli, M., Wiemer, S., 2016. The importance of earthquake interactions for injection-induced seismicity: retrospective modeling of the basel enhanced geothermal system. Geophys. Res. Lett. 43, 4992–4999.
Chanchani, S.K., Zoback, M.D., Barton, C., 2003. A case study of hydrocarbon transport along active faults and production-related stress changes in the Monterey Formation, California. In: In: Ameen, M. (Ed.), Fracture and In-Situ Stress Characterization of Hydrocarbon Reservoirs, Special Publication, vol. 209. Geological Society London, pp. 17–26.
Coulomb, C.A., 1773. Application des règles de maxima et minima à quelques problèmes de statique relatifs a l'Architecture. Acad. R. Sci. Mem. Math. Phys. 7, 343–528.
Das, S., Scholz, C.H., 1983. Why large earthquakes do not nucleate at shallow depths. Nature 35.
Dieterich, J.H., Richards-Dinger, K.B., Kroll, K.A., 2015. Modeling injection-induced seismicity with the physics-based earthquake simulator RSQSim. Seismol. Res. Lett. 86 (July/August (4)).
Ellis, B.R., Fitts, J.P., Bromhal, G.S., McIntyre, D.L., Tappero, R., Peters, C.A., 2013. Dissolution-driven permeability reduction of a fractured carbonate caprock. Environ.

Eng. Sci. 30 (4), 187–193. http://dx.doi.org/10.1089/ees.2012.0337.
Fang, Y., den Hartog, S.A.M., Elsworth, D., Marone, C., Cladouhos, T., 2016. Anomalous distribution of microearthquakes in the Newberry geothermal reservoir: mechanisms and implications. Geothermics 63, 62–73. http://dx.doi.org/10.1016/j.geothermics.2015.04.005.
Fang, Y., Elsworth, D., Wang, C., Ishibashi, T., Fitts, J.P., 2017. Frictional stability-permeability relationships for fractures in shales. J. Geophys. Res. Solid Earth 122 (3), 1760–1776. http://dx.doi.org/10.1002/2016JB013435.
Figueiredo, B., Tsang, C.F., Rutqvist, J., Bensabat, J., Niemj, A., 2015. Coupled hydro-mechanical processes and fault reactivation induced by CO2 Injection in a three-layer storage formation. Int. J. Greenh. Gas Control 39, 432–448.
Gischig, V.S., Wiemer, S., 2013. A stochastic model for induced seismicity based on non-linear pressure diffusion and irreversible permeability enhancement. Geophys. J. Int. 194 (2), 1229–1249.
Goertz-Allmann, B.P., Edwards, B., Bethmann Deichmann, N., Clinton, J., Ëah, D., Giardini, D., 2011. A new empirical magnitude scaling relation for Switzerland. Bull. Seismol. Soc. Am. 101, 3088–3095.
Gutenberg, B., Richter, C.R., 1954. Magnitude and energy of earthquakesx. Ann. Geof. 9, 1–15.
Hanks, T.H., Kanamori, H., 1979. A moment magnitude scale. J. Geophys. Res. 84 (B5), 2348–2350.
ITASCA, 2011. FLAC3d v5.0, Fast Lagrangian Analysis of Continua in 3 Dimensions, User's Guide. Itasca Consulting Group, Minneapolis, MN, USA.
Jaeger, J., Cook, N., Zimmerman, R., 2007. Fundamentals of Rock Mechanics, 4th ed. Blackwell Publishers, Oxford.
Jeanne, P., Guglielmi, Y., Lamarche, J., Cappa, F., Marié, L., 2012. Architectural characteristics and petrophysical properties evolution of a slip fault zone affecting fractured porous carbonate layers. J. Struct. Geol. 44, 93–109.
Jeanne, P., Guglielmi, Y., Cappa, F., Rinaldi, A.P., Rutqvist, J., 2014. The effects of lateral property variations on fault-zone reactivation by fluid pressurization: application to CO_2 pressurization effects within major and undetected fault zones. J. Struct. Geol. 62, 97–108.
Jeanne, P., Rutqvist, J., Wainwright, H.M., Foxall, W., Bachmann, C., Zhou, Q., Rinaldi, A.P., Birkholzer, J., 2016. Effects of in-situ stress measurement uncertainties on the assessment of the predicted seismic activity and risk associated with a hypothetical industrial-scale geologic CO_2 sequestration operation. J. Rock Mech. Geotech. Eng. 8, e873–e885.
Jolliffe, I.T., 2002. Principal Component Analysis, 2nd edition. Springer.
Kanamori, H., Brodsky, E.E., 2004. The physics of earthquakes. Rep. Prog. Phys. 67 (8), 1429.
Kohli, A.H., Zoback, M.D., 2013. Frictional properties of shale reservoir rocks. J. Geophys. Res. Earth 118 (9), 5109–5125. http://dx.doi.org/10.1002/Jgrb.50346.
Lockner, D.A., Beeler, N.M., 2002. Rock failure and earthquakes. In: Lee, W.H.K. (Ed.), International Handbook of Earthquake and Engineering Seismology. Academic Amsterdam, pp. 505–537.
Mair, K., Marone, C., 1999. Friction of simulated fault gouge for a wide range of velocity and normal stresses. J. Geoph. Res. 104 (28), 899–988 914.
Marone, C., 1998. Laboratory-derived friction laws and their application to seismic faulting. Annu. Rev. Earth Planet. Sci. 26, 643–696.
Mazzoldi, A., Rinaldi, A.P., Borgia, A., Rutqvist, J., 2012. Induced seismicity within geological carbon sequestration projects: maximum earthquake magnitude and leakage potential from undetected faults. Int. J. Greenh. Gas Control 10, 434–442.
McClure, M.W., Horne, R.N., 2011. Investigation of injection induced seismicity using a coupled fluid flow and rate/state friction model. Geophysics 76 (6), WC181–WC198.
Moore, D.E., Lockner, D.A., 2007. Friction of the smectite clay montmorillonite: a review and interpretation of data. In: In: Dixon, T.H., Moore, J.C. (Eds.), The Seismogenic Zone of Subduction Thrust Faults, MARGINS Theor. Exp. Earth Sci. Ser., vol. 2. Columbia Univ. Press, New York, pp. 317–345.
Morrow, C., Solum, J., Tembe, S., Lockner, D., Wong, T.F., 2007. Using drill cutting separates to estimate the strength of narrow shear zones at SAFOD. Geophys. Res. Lett. 34, L11301. http://dx.doi.org/10.1029/2007GL029665.
National Research Council, 2012. Induced Seismicity Potential in Energy Technologies. The National Academies Press, Washington, D.C.
Pacala, S., Socolow, R., 2004. Stabilization wedges: solving the climate problem for the next 50 years with current technologies. Science 13305 (5686), 968–972.
Pruess, K., Oldenburg, K., Moridis, G., 2012. TOUGH2 User's Guide, Version 2.1, LBNL-43134 (revised). Lawrence Berkeley National Laboratory, Berkeley, CA, USA.
Pruess, K., 2005. ECO2N: A TOUGH2 Fluid Property Module for Mixtures of Water, NaCl and CO_2, Report LBNL-57952. Lawrence Berkeley National Laboratory, Berkeley, CA, USA.
Rinaldi, A.P., Jeanne, P., Rutqvist, J., Cappa, F., Guglielmi, Y., 2014. Effects of fault-zone architecture on earthquake magnitude and gas leakage related to CO 2 injection in a multi-layered sedimentary system. Greenh. Gas Sci. Technnol. 4, 99–120.
Rutqvist, J., Cappa, F., Rinaldi, A.P., Godano, M., 2014. Modeling of induced seismicity and ground vibrations associated with geological CO_2 storage, and assessing their effects on surface structures and human perception. Int. J. Greenh. Gas Control 24, 64–77.
Rutqvist, J., Rinaldi, A.P., Cappa, F., Jeanne, P., Mazzoldi, A., Urpi, L., Guglielmi, Y., Vilarrasa, V., 2016. Fault activation and induced seismicity in geologic carbon storage − Lessons learned from recent modeling studies. J. Rock Mech. Geotech. Eng. 8, 789–804.
Rutqvist, J., 2011. Status of the TOUGH-FLAC simulator and recent applications related to coupled fluid flow and crustal deformations. Comput. Geosci. 37, 739–750.
Shapiro, S.A., Dinske, C., Kummerow, J., 2007. Probability of a given magnitude earthquake induced by a fluid injection. Geophys. Res. Lett. 34, L22314. http://dx.doi.org/10.1029/2007GL031615.
Solum, J.G., Hickman, S.H., Lockner, D.A., Moore, D.E., van der Pluijm, B.A., Evans, J.P., 2006. Mineralogical characterization of protolith and fault rocks from the SAFOD main hole. Geophys. Res. Lett. 33, L21314. http://dx.doi.org/10.1029/2006GL027285.
Tembe, S., Lockner, D.A., Wong, F., 2010. Effect of clay content and mineralogy on frictional sliding behavior of simulated gouges: binary and ternary mixtures of quartz, illite, and montmorillonite. J. Geophys. Res. 115, B03416. http://dx.doi.org/10.1029/2009JB006383.
van Genuchten, M.T., 1980. A closed-form equation for predicting the hydraulic conductivity of unsaturated soils. Soil Sci. Soc. Am. J. 44 (5), 892–898.
Wagoner, J.L., 2009. 3D Geologic Modeling of the Southern San Joaquin Basin for the Westcarb Kimberlina Demonstration Project-A Status Report.
Wainwright, H.M., Finsterle, S., Zhou, Q., Birkholzer, J.T., 2013. Modeling the performance of large-scale CO_2 storage systems: a comparison of different sensitivity analysis methods. Int. J. Greenh. Gas Control 17, 189–205.
Wang, C., Elsworth, D., Fang, Y., 2017. Influence of weakening minerals on ensemble strength and slip stability of faults. J. Geophys. Res. Solid Earth. http://dx.doi.org/10.1002/2016JB013687.
Zhang, K., Wu, Y.S., Pruess, K., 2008. User's Guide for TOUGH2-MP—A Massively Parallel Version of the TOUGH2 Code, Report LBNL-315E. Lawrence Berkeley National Laboratory, Berkeley, CA, USA.
Zhou, Q., Birkholzer, J.T., 2011. On scale and magnitude of pressure buildup induced by large-scale geologic storage of CO_2. Greenh. Gases Sci. Technol. 1, 11–20.
Zoback, M.D., Gorelick, S.M., 2012. Earthquake triggering and large-scale geologic storage of carbon dioxide. Proc. Natl. Acad. Sci. U. S. A. 109 (26), 10164–10168.